





Combined speckle- and propagation-based single shot two-dimensional phase retrieval method

ANDREW F. T. LEONG,¹  DANIEL S. HODGE,²  KELIN KURZER-OGUL,^{1,3} STEFANO MARCHESINI,⁴ SILVIA PANDOLFI,^{4,5} YANWEI LIU,⁴  JOHN L. BARBER,¹ KENAN LI,⁴  ANNE SAKDINAWAT,⁴ ERIC C. GALTIER,⁴ BOB NAGLER,⁴ HAE JA LEE,⁴ ERIC F. CUNNINGHAM,⁴  THOMAS E. CARVER,⁶ HUSSEIN ALUIE,^{3,7,8} JESSICA K. SHANG,^{3,6} CYNTHIA A. BOLME,¹ KYLE J. RAMOS,¹ DIMITRY KHAGHANI,⁴  RICHARD L. SANDBERG,²  DAVID S. MONTGOMERY,^{1,†} PAWEŁ M. KOZŁOWSKI,^{1,†} AND ARIANNA E. GLEASON^{9,*},[†]

¹Los Alamos National Laboratory, Los Alamos, New Mexico 87545, USA

²Department of Physics and Astronomy, Brigham Young University, Provo, Utah 34602, USA

³Department of Mechanical Engineering, University of Rochester, Rochester, New York 14623, USA

⁴SLAC National Accelerator Laboratory, 2575 Sand Hill Rd., Menlo Park, California 94025, USA

⁵IMPMC, Sorbonne University, Paris 75006, France

⁶Stanford Nano Shared Facilities, Stanford University, Stanford, California 94305, USA

⁷Laboratory for Laser Energetics, University of Rochester, Rochester, New York 14623, USA

⁸Department of Mathematics, University of Rochester, Rochester, New York 14623, USA

⁹Earth and Planetary Science, Stanford University, Stanford, California 94305, USA

[†]These authors contributed equally.

*ariannag@stanford.edu

Abstract: Single-shot two-dimensional (2D) phase retrieval (PR) can recover the phase shift distribution within an object from a single 2D x-ray phase contrast image (XPCI). Two competing XPCI imaging modalities often used for single-shot 2D PR to recover material properties critical for predictive performance capabilities are: speckle-based (SP-XPCI) and propagation-based (PB-XPCI) XPCI imaging. However, PR from SP-XPCI and PB-XPCI images are, respectively, limited to reconstructing accurately slowly and rapidly varying features due to noise and differences in their contrast mechanisms. Herein, we consider a combined speckle- and propagation-based XPCI (SPB-XPCI) image by introducing a mask to generate a reference pattern and imaging in the near-to-holographic regime to induce intensity modulations in the image. We develop a single-shot 2D PR method for SPB-XPCI images of pure phase objects without imposing restrictions such as object support constraints. It is compared against PR methods inspired by those developed for SP-XPCI and PB-XPCI on simulated and experimental images of a thin glass shell before and during shockwave compression. Reconstructed phase maps show improvements in quantitative scores of root-mean-square error and structural similarity index measure using our proposed method.

© 2024 Optica Publishing Group under the terms of the [Optica Open Access Publishing Agreement](#)

1. Introduction

Propagation-based x-ray phase contrast imaging (PB-XPCI) and speckle-based x-ray phase contrast imaging (SP-XPCI) are two XPCI modalities commonly employed for dynamically imaging weakly attenuating objects because of their simplistic setups and relaxed requirement on temporal coherence [1–4]. Often, one would perform 2D PR on single XPCI images recorded

from these imaging modalities to reconstruct the 2D phase shift distribution in the object (*phase object*) before converting the phase object into quantitative measures such as areal density, material composition, and particle size distribution [2,5,6]. Broadly speaking, phase retrieval of SP-XPCI images can uniquely reconstruct well up to a constant large-scale features (e.g., x-ray wavefronts [7]), whereas that of PB-XPCI images can reconstruct effectively but not uniquely small-scale features (e.g., material interfaces [8]) [9]. Moreover, like SP-XPCI imaging, differential-based (DF) XPCI imaging methods, such as coded-apertures XPCI [10], x-ray grating interferometry [11,12] and analyzer-based XPCI [13], are also limited in accuracy to reconstructing large-scale features. We leverage the advantages of both SP-XPCI & PB-XPCI to accurately reconstruct objects with small and large scale features by developing a combined speckle- and propagation-based phase retrieval (SPB-PR) technique which will be described herein.

Developing a PR method that can recover phase objects with features (or equivalently, phase gradients) spanning multiple length scales is widely inspired by the expanding field of research that uses XPCI to understand material response to sub-shock [4,6,14,15] and shock loading conditions [16,17]. These research efforts are important for testing and optimizing material performance under extreme conditions for space exploration, global defense and fusion energy. In particular, Inertial Confinement Fusion (ICF) and Inertial Fusion Energy (IFE) science and technology developments are an exciting area of research as a future source of clean energy [18]. In ICF, a target comprising of a shell filled with hydrogen fusion fuel is irradiated via laser beams to rapidly heat the outermost layer of the shell (ablator) and generate implosive shock waves that compress and heat the fusion fuel to thermonuclear conditions [19]. Voids in the ablation layer, however, collapse under the imploding shock and can seed Rayleigh-Taylor instabilities. This in turn leads to asymmetric compression and injection of ablator material into the fuel, degrading the efficiency of fusion reactions [20]. This has motivated concerted efforts using XPCI to observe, quantify, and computationally model void collapse with the aim of mitigating or possibly leveraging its effect in ICF [21,22].

Recently, single x-ray pulse XPCI imaging at X-ray free electron lasers (XFELs) has been demonstrated studying cavitation dynamics of bubble collapse [23] and water jet break-up [8], both from pulsed laser interaction with fluids. Successful single-pulse, near-field to holographic x-ray imaging was demonstrated in both cases by retrieval of dynamic phase and areal density images. However, all XFEL near-field to holographic imaging share similar challenges and solutions, such as flat-fielding and noise removal from XFEL self-amplified spontaneous emission (SASE) sources. Moreover, this work is imaging a strong planar laser shock in a solid sample compared to the laser-induced bubble or jet break up in fluids. This presents a unique set of challenges, such as large phase gradients (phases changes > 30 radians over a few microns appear in this work compared to over a few radians in the fluid examples) [8,23]. As result, multiple length scales and, therefore phase gradients, are created in the material ranging from slowly varying release wave-induced density gradients to rapidly varying hydrodynamic instabilities.

In the remainder of this paper, we demonstrate how SPB-XPCI can be used to image quantitatively the phase shift due to a shockwave interacting with a void and comparison to hydrodynamic simulations. Section 2 provides the theoretical model and numerical implementation of our combined SPB-PR method. This is validated with simulated and recorded XPCI images of a thin micron glass shell embedded in epoxy collapsing under a shock wave from the Matter in Extreme Conditions (MEC) instrument at the Linac Coherent Light Source (LCLS) (see Section 3 for details). In Section 4, phase object maps reconstructed from SPB-PR are compared with two PR methods inspired by those developed for PB-XPCI [24] and SP-XPCI [2] imaging, and then concluding with Section 5.

2. XPCI imaging modalities

2.1. PB-XPCI

A generic setup for PB-XPCI is shown in Fig. 1. Spatially coherent monochromatic x-ray plane waves propagating along the z -axis are focused by a compound refractive lens (CRL) over focal length F_L . Cone beam x-rays emerge from the focal point and travel distance R_1 to an x-ray transparent object. The object distorts the wavefield of the x-ray beam, which manifests into Fresnel diffraction fringes as it travels over distance R_2 and is recorded by the detector over the $\mathbf{r}_\perp = (x, y)$ -plane. These fringes are responsible for the enhanced contrast in PB-XPCI images, particularly at sample edges and interfaces where the x-ray wavefront is significantly distorted. Here, PB-XPCI uses free-space propagation of coherent x-rays to create *propagation-induced* phase contrast.

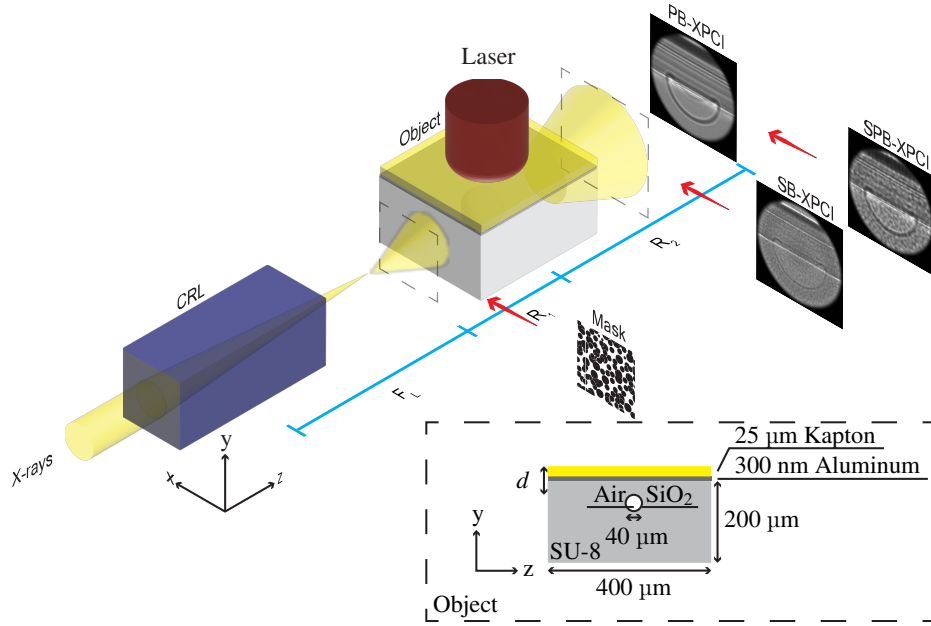


Fig. 1. PB-XPCI, SP-XPCI and SPB-XPCI imaging setups with cone beam x-rays produced by a compound refractive lens (CRL) in a laser-driven shock compression experiment. Inset: A 1 μm thick, 40 μm inner diameter SiO₂ dry air-filled shell embedded in a photoresist, SU-8. d is the distance from the air/kapton to the SU-8/SiO₂ shell interface.

Under the operator theory of coherent x-ray imaging, the PB-XPCI image $I_{W+O}(\mathbf{r}_\perp, z_{eff})$ recorded by the detector at an effective propagation distance $z_{eff} = R_1 R_2 / (R_1 + R_2)$ from the exit surface of the object located at $z = 0$ can be related to the object scalar wavefield $\Psi_O(\mathbf{r}_\perp, 0)$ (i.e., transmission function [25]) via:

$$I_{W+O}(\mathbf{r}_\perp, z_{eff}) = I_W(\mathbf{r}_\perp, z_{eff}) |H\Psi_O(\mathbf{r}_\perp, 0)|^2 \quad (1)$$

where

$$\Psi_O(\mathbf{r}_\perp, 0) = \exp(i\varphi_O(\mathbf{r}_\perp, 0)). \quad (2)$$

$I_W(\mathbf{r}_\perp, z_{eff})$ is the XPCI image in the absence of the object (white field), $I_O(\mathbf{r}_\perp, z_{eff}) = |H\Psi_O(\mathbf{r}_\perp, 0)|^2$ is the white field corrected XPCI image of the object, i is the complex number, and

$$H = \mathcal{F}^{-1} \exp\left(iz_{eff}\sqrt{k^2 - \mathbf{k}_\perp^2}\right) \mathcal{F} \quad (3)$$

is the free-space propagator where the paraxial approximation was assumed to invoke the Fresnel scaling theorem and allow z_{eff} to be included in H [26]. \mathcal{F} and \mathcal{F}^{-1} are the forward and inverse Fourier transforms with respect to spatial axes (x, y) and spatial frequencies $\mathbf{k}_\perp = (k_x, k_y)$, respectively. (k_x, k_y) are Fourier coordinates corresponding to the vectors (x, y) in real space, $k = 2\pi/\lambda$ is the wavenumber, and λ is the x-ray wavelength. In arriving at Eq. (1), it is assumed that the wavefield corresponding to $I_W(\mathbf{r}_\perp, z_{eff})$ is sufficiently slowly varying to negligibly perturb the phase object $\varphi_O(\mathbf{r}_\perp, 0)$. A more detailed explanation is provided in Section S2 (Supplement 1) on how this assumption leads to Eq. (1).

Propagation-based phase retrieval (PB-PR) aims to solve Eq. (1) (or some other equivalent form, for example, Kirchhoff's diffraction formula [27]) to determine $\varphi_O(\mathbf{r}_\perp, 0)$. Often, however, a single image is insufficient to uniquely solve for φ_O from Eq. (1), making it an ill-posed inverse problem [28]. As a result, a number of approaches to convert Eq. (1) into a regularized inversion have been proposed. These approaches can be divided into approximating H , e.g., linearizing the transport-of-intensity (TIE) or Fokker-Planck (FP) equation [29–31], and/or $\Psi_O(\mathbf{r}_\perp, 0)$, e.g., phase-attenuation duality (PA) [32], contrast transfer function (CTF) [33], projection approximation [26], object support constraint [25], object smoothness [34], phase/absorption object constraints [35], single material [36], and two material [37]. Such approximations have led to analytical, iterative, and deep learning methods for solving $\Psi_O(\mathbf{r}_\perp, 0)$.

In theory, the validity range of PB-PR is dictated by the approximations made in H and $\Psi_O(\mathbf{r}_\perp, 0)$. But in practice, PB-XPCI images are contaminated with noise that further reduces their validity range to spatially rapidly varying phase objects (i.e., features that occupy the holographic regime when Fresnel number $F = a/(z_{eff}\lambda|\nabla\varphi_O(\mathbf{r}_\perp, 0)|_{\max}) \leq 1$ [38], where a is the characteristic length scale of the object) (Fig. 2). This is because $I_O(\mathbf{r}_\perp, z_{eff})$ is approximately proportional to $\nabla_\perp^2\varphi_O(\mathbf{r}_\perp, 0)$ for slowly varying phases (see Eq. (11) in [39]). Consequently, for parts of the object where the phase object is slowly varying and the object is weakly attenuating, the PB-XPCI image intensity is minimally perturbed and thus easily lost under image noise.

2.2. SP-XPCI

SP-XPCI adds a mask to the PB-XPCI setup in Fig. 1 to generate a high frequency intensity reference pattern at the detector. z_{eff} is often strategically reduced (and/or x-ray energy increased) to minimize propagation-induced intensity contrast. Regular grids, sandpaper and particles are some examples of masks that have been successfully employed in SP-XPCI [42,43]. When an object is placed in front of the mask, the reference pattern is distorted. Distortion of the reference pattern, or *speckle-induced* phase contrast, is the underlying contrast mechanism that SP-XPCI relies on to retrieve the phase object.

To relate the phase object to its SP-XPCI image, we begin by expressing the x-ray wavefield $\Psi_{O+M}(\mathbf{r}_\perp, 0)$ in the presence of both the object (O) and mask (M) as:

$$\Psi_{O+M}(\mathbf{r}_\perp, 0) = \Psi_O(\mathbf{r}_\perp, 0)\Psi_M(\mathbf{r}_\perp, 0), \quad (4)$$

where

$$\Psi_M(\mathbf{r}_\perp, 0) = \exp(-A_M(\mathbf{r}_\perp, 0) + i\varphi_M(\mathbf{r}_\perp, 0)). \quad (5)$$

$A_M(\mathbf{r}_\perp, 0)$ and $O_M(\mathbf{r}_\perp, 0)$ are the absorbance and phase of the mask, respectively. To arrive at Eq. (4), the projection approximation was assumed within the object [26].

If $\varphi_O(\mathbf{r}_\perp, 0)$ has a local radius of curvature $R \gg R_2$ (i.e., the object is imaged well within the near-field regime, $F \gg 1$), and $\Psi_M(\mathbf{r}_\perp, 0)$ contains only high frequencies, then Eq. (1) can be approximated as [44]:

$$I_{W+O+M}(\mathbf{r}_\perp, z_{eff}) = I_W(\mathbf{r}_\perp, z_{eff}) |H\Psi_{O+M}(\mathbf{r}_\perp, 0)|^2 \quad (6a)$$

$$\approx I_W(\mathbf{r}_\perp, z_{eff}) \left[I_M(\mathbf{r}_\perp, z_{eff}) - \frac{z_{eff}}{k} \nabla_\perp \varphi_O(\mathbf{r}_\perp, 0) \cdot \nabla I_M(\mathbf{r}_\perp, z_{eff}) \right] \quad (6b)$$

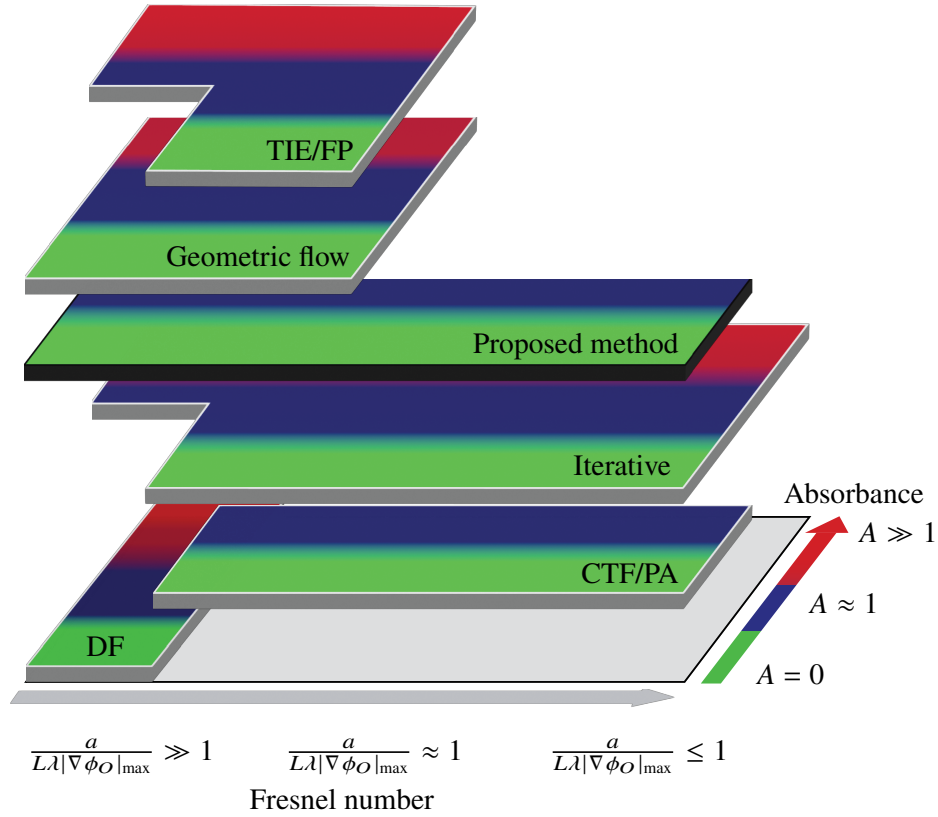


Fig. 2. Validity range of PB-PR (TIE/FP [31,36], Iterative [25,34,35], CTF/PA [32,33]), speckle-based phase retrieval (SP-PR) (DF [2,10–12], Geometric flow [5,40]) and our proposed SPB-PR method over the Fresnel number (ranging from the near-field to holographic regime) and absorbance of the object imaged. DF = Differential-based XPCI methods. FP = Fokker-Planck equation. TIE = Transport-of-intensity equation. Iterative = Methods that recast Eq. (1) into an optimization problem and apply constraints on $\Psi_O(\mathbf{r}_\perp, 0)$ such as in [41]. CTF = Contrast transfer function. PA = Phase-Attenuation duality. SPB-PR (Proposed method) is the only one that can adequately cover the near-field and holographic regimes.

where

$$I_M(\mathbf{r}_\perp, z_{\text{eff}}) = |\Psi_M(\mathbf{r}_\perp, z_{\text{eff}})|^2. \quad (7)$$

$\nabla_\perp = (\partial/\partial x, \partial/\partial y)$ is the directional derivative along the (x, y) -plane, and $I_{O+M} = |H\Psi_{O+M}(\mathbf{r}_\perp, 0)|^2$ is the white field corrected XPCI image of the combined object and mask. If we further assume that $\frac{z_{\text{eff}}}{k} \nabla_\perp \varphi_O(\mathbf{r}_\perp, 0) \cdot \nabla I_M(\mathbf{r}_\perp, z_{\text{eff}}) \ll 1$, then the following Taylor expansion truncated after the first order can be made:

$$I_M\left(\mathbf{r}_\perp - \frac{z_{\text{eff}}}{k} \nabla_\perp \varphi_O(\mathbf{r}_\perp, 0), z_{\text{eff}}\right) \approx I_M(\mathbf{r}_\perp, z_{\text{eff}}) - \frac{z_{\text{eff}}}{k} \nabla_\perp \varphi_O(\mathbf{r}_\perp, 0) \cdot \nabla I_M(\mathbf{r}_\perp, z_{\text{eff}}) \quad (8)$$

to arrive at:

$$I_{W+O+M}(\mathbf{r}_\perp, z_{\text{eff}}) \approx I_W(\mathbf{r}_\perp, z_{\text{eff}}) I_M\left(\mathbf{r}_\perp - \frac{z_{\text{eff}}}{k} \nabla_\perp \varphi_O(\mathbf{r}_\perp, 0), z_{\text{eff}}\right). \quad (9)$$

In Eq. (9), $I_{W+O+M}(\mathbf{r}_\perp, z_{\text{eff}})$ is related to $I_M(\mathbf{r}_\perp, z_{\text{eff}})$ by a deformation field proportional to $\nabla_\perp \varphi_O(\mathbf{r}_\perp, 0)$ [44]. This makes SP-XPCI much more sensitive to slowly spatially varying phase objects than PB-XPCI, which, as mentioned in Section 2.1, is sensitive to $\nabla_\perp^2 \varphi_O(\mathbf{r}_\perp, 0)$. The basic

approach of SP-PR is computing the deformation field using the reference pattern as control points to perform image registration between the white field corrected $I_M(\mathbf{r}_\perp, z_{eff})$ and $I_{O+M}(\mathbf{r}_\perp, z_{eff})$. Then, the deformation field is integrated to obtain a unique solution up to a constant for $\varphi_O(\mathbf{r}_\perp, 0)$ [2,3,45].

When the object is imaged beyond the very near-field regime (i.e., $F \gg 1$), propagation-induced phase contrast appears in the XPCI image and therefore SP-PR becomes inaccurate. To account for propagation-induced phase contrast, Wang *et al.* [46] described a technique for recording an XPCI image of the object with and without the reference pattern. However, it cannot be used for single-shot dynamic imaging. Paganin *et al.* [5] developed a geometric flow approach to incorporate free-space induced phase contrast by treating the reference pattern, distorted by a pure phase object, as a conserved current. Pavlov *et al.* [40] extended the geometric flow method to attenuating objects. Another XPCI method similar to SP-XPCI that uses a single absorbing mask is also able to separate propagation- and speckle-induced intensity contrast [47]. However, these methods are not valid in the holographic regime (i.e., $F \leq 1$) and/or are error-prone to spatial variations in the white field. The latter can often be removed by normalizing the object image against the white field. However, this approach can fail to completely remove the white field when there is pulse-to-pulse stochastic variations in x-ray intensity and mean energy [4,8,48], or if the reference object is inseparable from the imaging system [22]. In the next section, we propose a method that is valid beyond the near-field regime and robust against non-uniform illuminating and stochastically varying x-ray beam intensity distributions and mean energy [48].

2.3. SPB-XPCI

In this work, we combine the fundamental principles of SP-XPCI and PB-XPCI introduced in Sections 2.1 and 2.2, respectively, to describe our SPB-PR method for retrieving the phase of a non-absorbing object from a single SPB-XPCI image that contains both speckle- and propagation-induced phase contrast within and up to the holographic regime. In this case, SPB-XPCI adds a mask to the PB-XPCI setup, as is the same for SP-XPCI, but in addition z_{eff} is set sufficiently large to produce propagation-induced phase contrast (Fig. 1). For the synthetic XPCI images in this work, the mask generated is a distribution of SiO₂ particles to simulate the speckle pattern in the experimental XPCI images. Further details on the generation of the mask is provided in Section 3.2.

$\varphi_O(\mathbf{r}_\perp, 0)$ is assumed to be an analytic function infinitely differentiable, and that there exists a convergent power series at every point \mathbf{r}_\perp in the plane perpendicular to z . Consequently, at every point \mathbf{r}_\perp the phase object can be Taylor expanded and decomposed into rapidly and slowly varying phase components $\varphi_{O_R}(\mathbf{r}_\perp, 0)$ and $\varphi_{O_S}(\mathbf{r}_\perp, 0)$, respectively:

$$\varphi_O(\mathbf{r}_\perp, 0) = \varphi_{O_S}(\mathbf{r}_\perp, 0) + \varphi_{O_R}(\mathbf{r}_\perp, 0), \quad (10)$$

such that $\nabla^n \varphi_{O_S}(\mathbf{r}_\perp, 0) = 0$ and $\nabla^n \varphi_O(\mathbf{r}_\perp, 0) = \nabla^n \varphi_{O_R}(\mathbf{r}_\perp, 0)$ for $n \geq 2$. Substituting Eqs. (10) and (2) into (4) gives the x-ray wavefield immediately after the object:

$$\Psi_{O+M}(\mathbf{r}_\perp, 0) = \Psi_M(\mathbf{r}_\perp, 0)\Psi_{O_R}(\mathbf{r}_\perp, 0)\Psi_{O_S}(\mathbf{r}_\perp, 0), \quad (11)$$

where $\Psi_{O_R}(\mathbf{r}_\perp, 0) = \exp(i\varphi_{O_R}(\mathbf{r}_\perp, 0))$ and $\Psi_{O_S}(\mathbf{r}_\perp, 0) = \exp(i\varphi_{O_S}(\mathbf{r}_\perp, 0))$.

The key observation to make in Eq. (11) is that $\Psi_{O_R}(\mathbf{r}_\perp, 0)$ and $\Psi_M(\mathbf{r}_\perp, 0)$ can be categorized together as containing only high frequency wavefield components, while $\Psi_{O_S}(\mathbf{r}_\perp, 0)$ contains only low frequency wavefield components. Equation (11) can be re-expressed as:

$$\Psi_{O+M}(\mathbf{r}_\perp, 0) = \Psi_{O_R+M}(\mathbf{r}_\perp, 0)\Psi_{O_S}(\mathbf{r}_\perp, 0), \quad (12)$$

where

$$\Psi_{O_R+M}(\mathbf{r}_\perp, 0) = \Psi_{O_R}(\mathbf{r}_\perp, 0)\Psi_M(\mathbf{r}_\perp, 0) \quad (13a)$$

$$= \exp(A_M(\mathbf{r}_\perp, 0) + i[\varphi_{O_R}(\mathbf{r}_\perp, 0) + \varphi_M(\mathbf{r}_\perp, 0)]). \quad (13b)$$

Substituting Eq. (12) into Eq. (6a) and assuming φ_{O_S} has a local radius of curvature of $R \gg R_2$, Eq. (6a) can be approximated as [44]:

$$I_{W+O+M}(\mathbf{r}_\perp, z_{eff}) \approx I_W(\mathbf{r}_\perp, z_{eff})I_{O_R+M}\left(\mathbf{r}_\perp - \frac{z_{eff}}{k}\nabla_\perp\varphi_{O_S}(\mathbf{r}_\perp, 0), z_{eff}\right) \quad (14a)$$

$$= I_W(\mathbf{r}_\perp, z_{eff})I_{O_R+M}(\mathbf{r}_\perp - \mathbf{D}_\perp, z_{eff}) \quad (14b)$$

where

$$\mathbf{D}_\perp = (D_x, D_y) = \frac{z_{eff}}{k}\nabla_\perp\varphi_{O_S}(\mathbf{r}_\perp, 0) \quad (15)$$

is the deformation field that maps $I_{O_R+M}(\mathbf{r}_\perp, z_{eff})$ to $I_{O+M}(\mathbf{r}_\perp, z_{eff})$, and is assumed to be $\ll 1$.

Equation (14b) represents an alternative expression of Eq. (6a) to propagating x-ray wavefields. Equation (6a) propagates the total x-ray wavefield to the detector plane via the propagator H , while Eq. (14a) propagates the rapidly varying components (O_R and M) via H , then distorts the resultant image with that of the slowly varying component (O_S). In other words, Eq. (14b) separates the components of the x-ray wavefield into high frequency components responsible for producing propagation-induced phase contrast (i.e., edge enhancement of the object and generation of reference pattern), and low frequency components (O_S) that produce speckle-induced phase contrast (i.e., distortion of the propagation-induced phase contrast). We also note the generality of Eq. (14b), assuming only that $\varphi_O(\mathbf{r}_\perp, 0)$ is analytic.

Finally, we introduce our combined SPB-PR method by minimizing the following three objective functions using, respectively, Eqs. (6a), (14b) and (15):

$$f_1(\varphi_O) = \left\| \sqrt{I_{O+M}(\varphi_O)} - \sqrt{\hat{I}_{O+M}} \right\|_2^2 + \lambda_1 \mathfrak{R}_1(\varphi_O) \quad (16a)$$

$$f_2(\mathbf{D}_\perp) = \left\| I_{O_R+M}(\mathbf{r}_\perp - \mathbf{D}_\perp) - \hat{I}_{O+M} \right\|_2^2 + \lambda_2 \mathfrak{R}_2(\mathbf{D}_\perp) \quad (16b)$$

$$f_3(\varphi_{O_S}) = \left\| w_x \left| \frac{z_{eff}}{k} \frac{\partial \varphi_{O_S}}{\partial x} - \hat{D}_x \right|^2 + w_y \left| \frac{z_{eff}}{k} \frac{\partial \varphi_{O_S}}{\partial y} - \hat{D}_y \right|^2 \right\|_2^2 \quad (16c)$$

where \hat{I}_{O+M} is the recorded white and dark field corrected XPCI image. $\|\cdot\cdot\|_2^2$ is the squared Euclidean 2-norm. $\hat{\mathbf{D}}_\perp = (\hat{D}_x, \hat{D}_y)$ is the displacement field that minimizes Eq. (16b). \mathfrak{R}_1 and \mathfrak{R}_2 are regularization functions weighted by constants λ_1 and λ_2 , respectively. w_x and w_y are space-dependent weight functions that assign values between $[0,1]$ in $\hat{\mathbf{D}}_\perp$ based on the uncertainty in the XPCI image intensity. For example, regions that are noisy due to low x-ray photon counts or x-ray scattering have greater uncertainty in $\hat{\mathbf{D}}_\perp$ and are therefore assigned smaller weights. Explicit dependence on \mathbf{r}_\perp and z_{eff} hereon will be dropped for notational simplicity.

Equation (16a) represents the PB-PR portion of our SPB-PR method by using the PB-XPCI forward model in Eq. (1). Ideally, minimizing Eq. (16a) alone reconstructs the phase object. However, as mentioned in Section 2.1, without sufficient prior information about the object, Eq. (16a) is an ill-posed minimization problem. Consequently, we supplement Eq. (16a) with Eqs. (16b) and (16c), the SP-PR portion of our SPB-PR method. Minimization of Eq. (16b) determines $\hat{\mathbf{D}}_\perp$ between I_{O_R+M} and \hat{I}_{O+M} , which Eq. (16c) then integrates with a weighted least squares method to determine φ_{O_S} . There are many ways to jointly solve Eqs. (16a)-(16c), some of which are discussed in Section 5. In our work, the following combination of numerical methods were implemented for minimizing the objective functions: momentum-based gradient descent with \mathfrak{R}_1 set to an approximation of the total variation (TV) regularizer (Eq. (16a)) [49], diffeomorphic demons registration that sets \mathfrak{R}_2 as a high-pass filter regularizer (Eq. (16b)) [50], and least squares minimization (Eq. (16c)) [2]. Further details of these numerical methods are described in Section S1 (Supplement 1).

3. Materials and methods

3.1. Sample

To study the shock-induced microstructural evolution of void collapse in an ICF ablator-type material, SU-8 photoresist epoxy (1.185 g/cm^3 ; Kayaku Advanced Materials) and SiO_2 shell (2.65 g/cm^3 [51]; Cospheric LLC) were selected as the proxy for the ablator material and engineered void, respectively (see inset in Fig. 1). While in actual ablators there is no glass shell, this design enabled higher precision in void placement and fine control over void size. We performed xRAGE simulations with and without the glass shell, and showed that they both displayed similar SU-8 behavior during the early stages of void collapse [52]. To fabricate ablator samples, SU-8 was spin coated to a thickness of $139 \text{ }\mu\text{m}$. Then, a $39 \pm 1.5 \text{ }\mu\text{m}$ inner diameter SiO_2 shell was placed on top and covered by an additional layer of SU-8. The sample was etched into a $0.4 \text{ mm} \times 0.2 \text{ mm} \times 2.5 \text{ mm}$ cuboid using photolithography. A 300 nm layer of aluminium (Al) and $25 \text{ }\mu\text{m}$ layer of black Kapton CB was added to the the SU-8 block with $d = 61 \text{ }\mu\text{m}$. Al provided a reflective layer for performing velocimetry measurements. Kapton was used as an ablator because of its well-known equation-of-state (EOS) and frequent use in laser-driven shockwave experiments [22,53,54]. For more details on how these samples were fabricated and characterized, see [52].

3.2. Experimental setup

All shock imaging experiments were conducted in the MEC instrument at LCLS. A 527 nm wavelength, $98 \text{ }\mu\text{m}$ super Gaussian (order 5.2) radius, 10 ns long laser pulse was delivered to the sample with a total energy of 75.2 J to generate a shock wave propagating towards the void. A single SPB-XPCI image was captured with a 18 keV (0.1% bandwidth) x-ray pulse focused by a beryllium compound refractive lens (Be-CRL) comprised of 95 individual lenses stacked with an effective focal length of $F_L = 278 \text{ mm}$. The sample was positioned $R_1 = 63.6 \text{ mm}$ from the focal point and a further $R_2 = 4.669 \text{ m}$ downfield was a $50 \text{ }\mu\text{m}$ thick LuAg:Ce scintillator coupled to a $2\times$ magnification objective lens and a $6.5 \text{ }\mu\text{m}$ pixel pitch Zyla camera. This produced an effective pixel size of 44.5 nm and $z_{\text{eff}} = 62.7 \text{ mm}$. Dust particles and defects in the Be-CRL formed speckles on the images, which we used as the reference pattern in lieu of inserting a mask in front of the Be-CRL as shown in Fig. 1. Further details on the experimental setup can be found in [55].

3.3. Simulation

Ideally, SPB-PR, SP-PR and PB-PR are assessed and compared on experimental XPCI images. However, their true phase object maps (*ground truths*) are not known. Thus, we generated highly realistic synthetic XPCI images for the purposes of testing our SPB-PR method. First, the sample was modeled as a $1 \text{ }\mu\text{m}$ thick, $40 \text{ }\mu\text{m}$ inner diameter SiO_2 shell embedded in a 0.2 mm diameter, 0.1746 mm long cylindrical block of SU-8 photoresist material. Deposited on the circular surface facing the laser beam is a 300 nm thick layer of Al and $25 \text{ }\mu\text{m}$ thick layer of Kapton CB ablator. The shell is centered on the rotating axis of the cylinder and $d = 55.2 \text{ }\mu\text{m}$. Low density dry-air ($1 \times 10^{-8} \text{ g/cm}^3$ [56]) surrounded the sample.

Laser shock compression of the sample was simulated using the xRAGE radiation-hydrodynamics code [57] while assuming axisymmetric flow around the rotating axis of the SU-8 cylinder. EOS models were obtained from the SESAME EOS library [58] (for SiO_2 and Al) and Livermore EOS library [59,60] (for SU-8 and Kapton). xRAGE outputted a time sequence of volumetric density maps for each material with a pixel size $0.1 \text{ }\mu\text{m}$. To save computation time, the volumetric density map for Al was not outputted and assumed to be vacuum. At a given time step, each material volume density map was multiplied by their complex refractive index, where the attenuation coefficient and refractive index decrement were tabulated from XOP [61]. The maps were summed and Abel transformed to calculate $\Psi_O(\mathbf{r}_\perp, 0)$, then propagated with a $31.2 \text{ }\mu\text{m}$ standard

deviation Gaussian x-ray beam to the detector plane at $z_{eff} = 62.7$ mm using the angular spectrum method to simulate its XPCI image [26]. These images were blurred with a pseudo-Voigt function to account for the point spread function (PSF) at MEC-LCLS, which includes the scintillator, finite source size and partial degree of transverse coherence of the x-ray beam (further details provided in Section S2 (Supplement 1)) [62]. Finally, added to the images was 5% Gaussian noise (compared to $\sim 3\%$ noise measured from experimentally recorded white fields).

To generate a speckled reference pattern, $\Psi_M(\mathbf{r}_\perp, 0)$ was simulated assuming the projection approximation from a computer-generated 84.5 μm thick vacuum-filled container with a 10% volume packing density of randomly distributed 1.6(x) $\mu\text{m} \times 1.6(y) \mu\text{m} \times 2.0(z) \mu\text{m}$ ellipsoidal SiO_2 particles. $\Psi_M(\mathbf{r}_\perp, 0)$ was multiplied with $\Psi_O(\mathbf{r}_\perp, 0)$ but the container of particles was not included in the xRAGE simulations since it was not in the path of the drive laser used for shock compression.

Although the SU-8 was modeled as a cylinder instead of a cuboid, the material response around the void is expected to be the same. Release waves reflecting off the SU-8 boundary for either sample geometry would not have reached the void when x-ray images were recorded during first shock wave arrival at the void. In addition, the imaging field-of-view (FOV) is much smaller than the radius of the cylindrical sample. Consequently, the SU-8 thickness along the x-ray direction for both the simulated and experimental object is approximately constant.

3.4. Image processing and analysis

XPCI images were dark field subtracted using recorded images of the detector dark current. Other image processing methods described in Section S3 (Supplement 1) were employed for SP-PR, PB-PR and SPB-PR. These include: (1) reversing image blur, (2) normalizing against the white field, (3) smoothing circular aperture, (4) aligning the speckle pattern between $I_{O+M}(\mathbf{r}_\perp, z_{eff})$ and $I_M(\mathbf{r}_\perp, z_{eff})$ for PB-PR, (5) solving Eq. (16c) over a circular aperture, (6) removing higher order Fresnel fringes and slowly varying intensity variations, (7) phase unwrapping, (8) offsetting reconstructed phase object by a constant, and (9) suppressing Fourier component of the phase at the Nyquist frequency.

The purpose for some of these image processing methods was to correct for the shot-to-shot stochastic variation in total photons, travelling direction and mean energy generated through SASE at LCLS [48]. To elaborate, recordings of the x-ray transverse beam profile are broadly single peak-shaped [11]. Consequently, shot-to-shot stochastic variations in total photons and travelling direction translate to changes in peak amplitude and position, respectively. To correct for these variations, $I_{W+O+M}(\mathbf{r}_\perp, z_{eff})$ and $I_{W+M}(\mathbf{r}_\perp, z_{eff})$ were normalized against the white field, $I_W(\mathbf{r}_\perp, z_{eff})$. $I_W(\mathbf{r}_\perp, z_{eff})$ was approximated by fitting Zernike polynomials to $I_{W+M}(\mathbf{r}_\perp, z_{eff})$ [63]. Since $I_{W+O+M}(\mathbf{r}_\perp, z_{eff})$ and $I_{W+M}(\mathbf{r}_\perp, z_{eff})$ were recorded with different x-ray pulses that have different peak amplitudes and positions, there are slowly varying intensities in the white field corrected $I_{O+M}(\mathbf{r}_\perp, z_{eff})$.

We observed that slow variations in x-ray intensity become rapid oscillations in φ_O close to the Nyquist frequency when minimizing f_1 (not shown). We suppressed these high frequencies by applying a median filter to φ_O , as described in Section S3 (Supplement 1). Conversely, slow variations in x-ray intensity become low frequency variations in φ_{O_s} when minimizing f_2 and f_3 due to the assumption in demons registration that intensity does change between $I_{O+M}(\mathbf{r}_\perp, z_{eff})$ and $I_M(\mathbf{r}_\perp, z_{eff})$. Consequently, XPCI images were divided by their Gaussian blurred version with a standard deviation of 20 pixels. This value was chosen to be much larger than the speckle size of the speckle pattern.

Stochastic variations in the x-ray mean energy causes the Be-CRL lens to vary in magnification and therefore expands/contracts the speckle pattern from its center. This adds a spherical phase front to φ_O . To remove this, $I_M(\mathbf{r}_\perp, z_{eff})$ was one of many recordings chosen whose speckle pattern best aligned with that of $I_{O+M}(\mathbf{r}_\perp, z_{eff})$ in the unshocked SU-8 region of the object. Only

a small region where the object phase gradient is zero was needed to compare the speckle pattern between the two images because the speckle pattern is globally distorted by the spherical phase front.

We benchmarked our SPB-PR algorithm against two PR algorithms inspired by those successfully used in SP-XPCI [2] and PB-XPCI [24]. The first of these inspired techniques is by Morgan *et al.* [2]. They used cross-correlation to calculate the speckle displacement field between SP-XPCI images with and without an object before performing least squares 2D integration of the displacement field to calculate φ_O . The second is by Wittwer *et al.* [24], who developed a constrained alternating projection approach to calculate φ_O from PB-XPCI images. Its novelty lies in calculating φ_O directly, rather than indirectly by calculating $\Psi_O(\mathbf{r}_\perp, 0)$. This allows phases $>2\pi$ to be recovered without phase unwrapping. To fairly assess our SPB-PR method, [2] and [24] were modified to remove any differences in performance due to the use of different numerical methods. For Morgan *et al.* [2], we switched from cross-correlation to diffeomorphic demons registration used in our SPB-PR method for minimizing f_2 [50]. For Wittwer *et al.* [24], we replaced the alternating projection approach with the momentum-based gradient descent used in our SPB-PR method for minimizing f_1 .

Phase maps reconstructed from simulated XPCI images were assessed using the normalized root-mean-square error (RMSE) as a pixel-by-pixel measure of accuracy, structural similarity index measure (SSIM) to quantify how well structural features were reconstructed (further details are provided in Section S4 (Supplement 1)), and reconstruction time (RT) to measure the time taken from pre-processing the XPCI images to reconstructing a single $844 \text{ pixel} \times 844 \text{ pixel}$ phase object. MATLAB with the Image Processing and Parallel Computing toolboxes were used to run all custom-developed phase reconstruction algorithms on a PC using a Intel Core Xeon W-10855M (6 Core, 12 MB, Cache, 2.80 GHz to 5.10 GHz, 45W, 12 CPUs), NVIDIA Quadro RTX 3000 w/6GB (36 GB shared memory) GDDR6 with 64GB, 2x32GB, DDR4 2933MHz Non-ECC memory [64].

4. Results and discussion

4.1. Comparison of synthetic and experimental XPCI images

Dark field corrected synthetic and experimental XPCI images of SiO_2 shell embedded in SU-8, along with their corresponding XPCI image of the mask, are shown in Figs. 3(a) and 3(b), and that of the same object shock compressed are displayed in Figs. 3(c) and 3(d), respectively. Immediately apparent is that the speckle pattern in the experimental image appears slightly smaller with sharper features than in the synthetic image. There are also features interspersed throughout the speckle pattern in the experimental image (one of which is marked by a blue arrow in Fig. 3(b)) that does not belong to the object but are likely from defects in the Be-CRLs. However, Aloisio *et al.* [43] showed that the size and contrast of the speckle pattern negligibly affect the accuracy of registering images. Thus, we expect that $\hat{\mathbf{D}}_\perp$ was computed with similar accuracy for both the synthetic and experimental images.

We note three other major differences between the synthetic and experimental XPCI images, these are located at the: (1) ablation front, (2) reflective layer and (3) secondary shocks. An explanation on possible sources of these differences is provided in Section S5 (Supplement 1). Notwithstanding these differences, the main features of a shock-void interaction are realistically represented in the synthetic XPCI image, including the: (1) Fresnel fringes of the primary shock front, which indicates the three-dimensional (3D) primary shock front profile is correctly simulated, (2) acceleration of a plasma jet ahead of the incident shock front, and (3) early formation of cavity lobes as a result of baroclinic vorticity induced by the orthogonal pressure gradient across the shock front and density gradient across the void/SU-8/ SiO_2 shell interfaces [21]. Thus, these features were the focus of benchmarking our SPB-PR method against the other two PR methods.

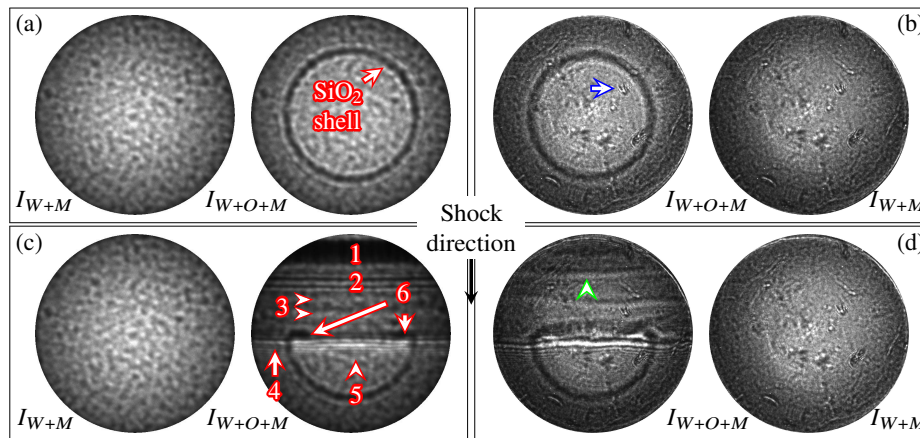


Fig. 3. $62.4 \mu\text{m} \times 62.4 \mu\text{m}$ dark field corrected XPCI images of a $1 \mu\text{m}$ thick, $40 \mu\text{m}$ inner diameter SiO_2 shell embedded in SU-8 (a) and (b) before and (c) and (d) after laser shock-induced compression, I_{W+O+M} . Each XPCI is accompanied with their speckle-only image, I_{W+M} . XPCI images in (a) and (c) are simulated using xRAGE [56], and (b) and (d) are recorded at MEC-LCLS. The primary and secondary shocks are moving from top to bottom. Blue arrow in (b) is pointing at a defect in the Be-CRL. Numbers in (c) label: (1) Ablation front, (2) Reflector, (3) Secondary shock fronts, (4) Primary shock front, (5) Jet and (6) Cavity lobes. Green arrow in (d) is pointing at a secondary shock.

Images from Fig. 3 were pre-processed as described in Section 3.4 before performing SP-PR, PB-PR and SPB-PR. Their pre-processed images are displayed in Section S6 (Supplement 1).

4.2. Phase retrieval of SiO_2 shell before shock compression

An xRAGE-simulated SiO_2 shell phase map is shown in Fig. 4(a). This corresponds to the XPCI image in Fig. 3(a) and from which phase maps are reconstructed with SP-PR, PB-PR and SPB-PR (Figs. 4(b)–4(d)). SP-PR reconstructs the void well, but not the SiO_2 shell. This is expected since the SiO_2 shell is dominated by propagation-induced phase contrast. Starting from a zero phase initial guess, both PB-PR and SPB-PR improve on reconstructing the SiO_2 shell. However, PB-PR fails to reconstruct the void because, as mentioned in section 2.1, for weakly attenuating objects it is much less sensitive to slowly-varying features. Others such as Wittwer *et al.* [24] and Latychevskaia and Fink [35] were able to overcome this insensitivity by imposing object support constraints but this is not applicable to objects without finite support. On the other hand, SPB-PR is able to reconstruct both the void and shell. Line profiles crossing the center of their phase maps along x (Fig. 5(a)) and y (Fig. 5(b)) further shows that SPB-PR overall combines the advantages of both SP-PR and PB-PR in reconstructing both slowly and rapidly varying features well.

Similarly, for phase maps reconstructed from the experimentally recorded XPCI image in Fig. 3(b) of a SiO_2 shell (Figs. 4(e)–4(g)), SP-PR accurately reconstructs only the void, PB-PR reconstructs well only the SiO_2 shell, and SPB-PR reconstructs both the shell and void. However, from their line profiles plotted in Figs. 5(c) and 5(d), the SU-8 phase on the left and right side of the SiO_2 shows a difference of up to ~ 1 radian. This represents the low frequency variations that can be seen in the reconstructed phase maps. Given that ~ 1 radian corresponds to a $\sim 15 \mu\text{m}$ variation in thickness across the SU-8 block, which is much larger than that measured using high resolution x-ray computed tomography [52], the low frequency variations are likely reconstruction artifacts rather than physical features of the sample. A potential source of this inaccuracy lies in the high frequency features that includes the reference speckle pattern and

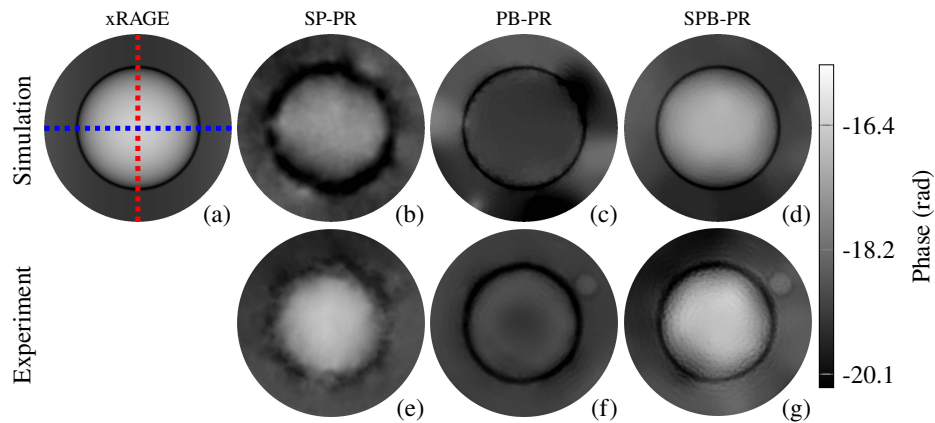


Fig. 4. (a) $62.4 \mu\text{m} \times 62.4 \mu\text{m}$ simulated SiO_2 shell phase map corresponding to the I_{W+O+M} in Fig. 3(a). PR performed on I_{W+O+M} in Fig. 3(a) using (b) SP-PR, (c) PB-PR and (d) SPB-PR. PR performed on the experimental XPCI image I_{W+O+M} in Fig. 3(b) using (e) SP-PR, (f) PB-PR and (g) SPB-PR. Blue and red dotted lines represent x and y line profiles, respectively, plotted in Fig. 5.

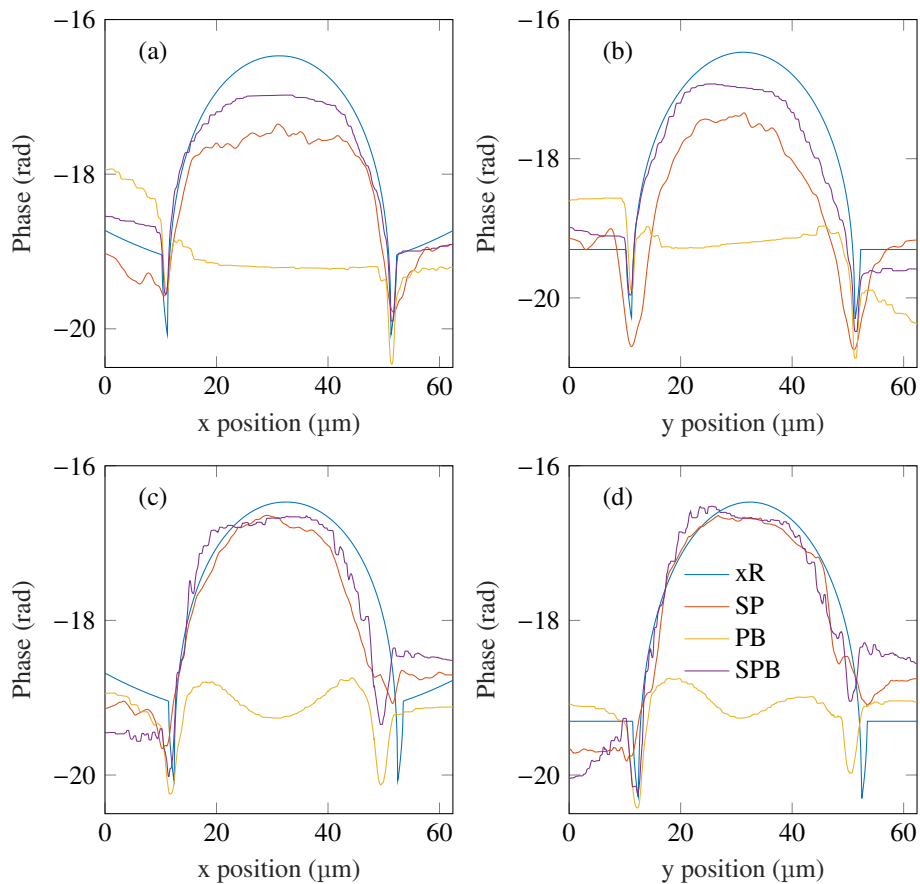


Fig. 5. Line profiles along (a) x and (b) y crossing the center of the phase maps in Figs. 4(a)–4(d). Line profiles along (c) x and (d) y crossing the center of the phase maps in Figs. 4(a), 4(e)–4(g).

SiO₂ shell. These are significantly blurred by the PSF. Since it is difficult to deconvolve the PSF in the presence of image noise, errors are introduced into $\hat{\mathbf{D}}_{\perp}$, which translates into low frequency artifacts in the phase object. Finally, the phase at the center of the void reconstructed from the experimental XPCI image match much more closely than from the simulated XPCI image to the xRAGE-simulated phase. A larger pixel size used in the simulation than in the experimental XPCI image may have made it difficult to detect the smaller shifts in the speckle pattern particularly towards the center of the void in the presence of image noise.

4.3. Phase retrieval of SiO₂ shell under shock compression

The synthetic SiO₂ shell in Fig. 4(a) was shock compressed using xRAGE and its resultant phase map is displayed in Fig. 6(a). Reconstruction of this phase map from its XPCI image (I_{W+O+M} in Fig. 3(c)) was performed using SP-PR, PB-PR and SPB-PR (Figs. 6(b)–6(d)). As expected, SP-PR fails to reconstruct small-scale features including the reflective layer, shock front and SiO₂ shell but reconstructs large-scale features including the void and shocked region of SU-8. On the other hand, PB-PR reconstructs small-scale features including the SiO₂ shell and, when the

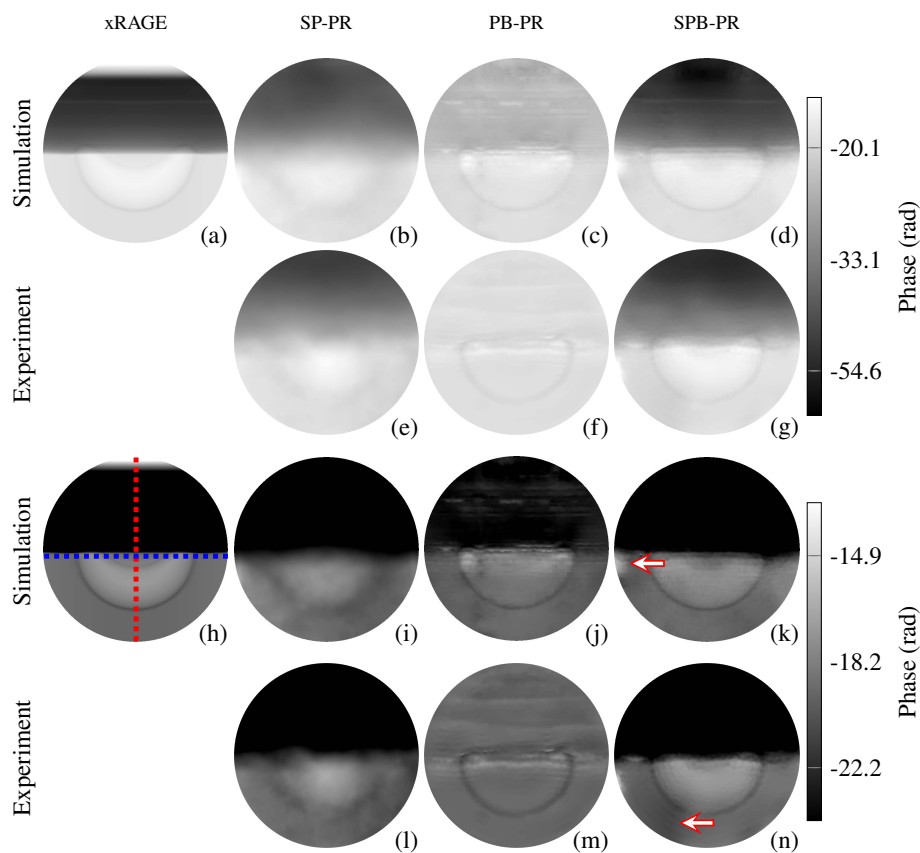


Fig. 6. (a) $62.4 \mu\text{m} \times 62.4 \mu\text{m}$ simulated laser-shock compressed SiO₂ shell phase map corresponding to I_{W+O+M} in Fig. 3(c). PR performed on I_{W+O+M} in Fig. 3(c) using (b) SP-PR, (c) PB-PR and (d) SPB-PR. PR performed on Fig. 3(d) using (e) SP-PR, (f) PB-PR and (g) SPB-PR. (h)–(n) correspond to (a)–(g) but with the grayscale color map range selected to emphasize phase values in front of the shock front. Red and blue dotted lines represent x and y line profiles, respectively, plotted in Fig. 7.

range of phase values on the color map is narrowed to the SiO₂ shell in Figs. 6(h)–6(k), jetting material. Again, SPB-PR reconstructs both the small- and large-scale features.

A closer inspection of the jetting material by plotting a horizontal line profile across it shows SPB-PR in close agreement with xRAGE (Fig. 7(a)). Similarly, a vertical line profile crossing the center of the phase maps reveals the shocked SU-8 region is most accurately reconstructed by SPB-PR. However, all three PR methods reconstruct poorly the ablation front. Based on our XPCI simulations of the ablation front showing multiple bright and dark horizontal Fresnel fringes, we suspect some of those fringes were recorded outside the x-ray beam's FOV. Generally, the number of fringes increases with phase steepness. As an example, the vertical line profile of the phase map simulated by xRAGE in Fig. 7(c) shows that the shock front has a much larger phase gradient than the SiO₂ shell. As a result, in the corresponding XPCI image (I_{W+O+M} in Fig. 3(c)), more Fresnel fringes are produced by the shock front than by the SiO₂ shell. Following on from this reasoning, the absence of the secondary fringes caused the PR methods to underestimate the phase steepness across the ablation front.

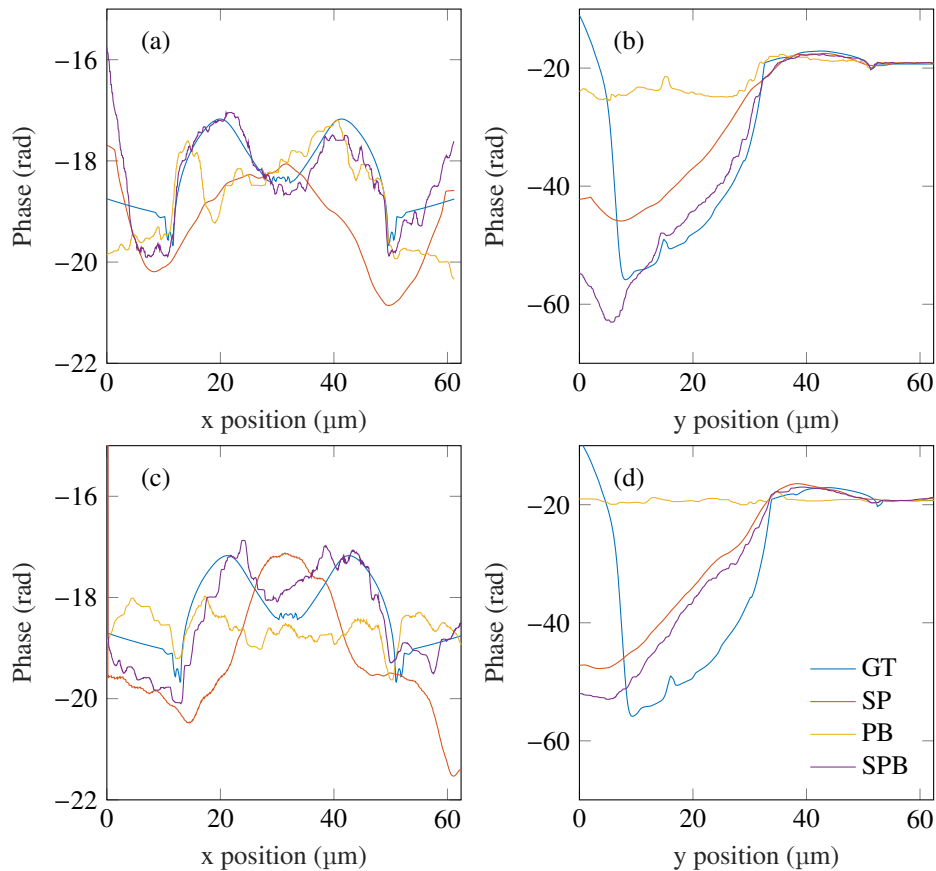


Fig. 7. Line profiles along (a) x and (b) y crossing the center of the phase maps in Figs. 6(a)–6(d). Line profiles along (c) x and (d) y crossing the center of the phase maps in Figs. 6(a), 6(e)–6(g).

Bright and dark patches in the reconstructed phase maps can be seen, which are marked by a red arrow in Figs. 6(k) and 6(n), respectively. These are caused by having set the TV regularization parameter λ_1 too high and thus over-smoothing the phase object. Because of this, its XPCI image does not sufficiently match in intensity to the recorded XPCI image. When these two images

are registered, $\hat{\mathbf{D}}_{\perp}$ is non-zero. As a consequence, bright/dark patches are formed and become increasingly bright/dark each time $\hat{\mathbf{D}}_{\perp}$ is computed since $\hat{\mathbf{D}}_{\perp}$ never converges to zero.

As a final comparison, the three PR methods were tested on an experimentally recorded XPCI image of a shock compressed SiO₂ shell (I_{W+O+M} in Fig. 3(d)). The reconstructed phase maps are shown in Figs. 6(e)–6(g) and line profiles across them in the x and y directions are shown in Figs. 7(c) and 7(d), respectively. The relative performance between the three PR methods are similar to when they were applied to the synthetic XPCI image of a shock compressed SiO₂ shell. SP-PR again fails to reconstruct the rapidly varying features including the SiO₂ shell, jet and lobes, but both PB-PR and SPB-PR are able to reconstruct them. However, SPB-PR can reconstruct as well the shock front and shocked region of the SU-8. Even so, there is still a significant discrepancy between SPB-PR and xRAGE in the shocked regions of the SU-8 (compare the phase values between 10 μm and 35 μm in Fig. 7(d)). This discrepancy may be because xRAGE did not account for laser plasma instabilities, which affects the shock front profile. On the other hand, the pseudo-Voigt function may not have been a sufficiently accurate estimate of the PSF for deconvolving the Fresnel fringes, leading to SPB-PR overestimating the phase in the shocked regions of the SU-8. It would be pertinent in future experiments to directly measure the PSF experimentally using, for example, the slanted-edge method [65].

4.4. Numerical comparison between PB-PR, SP-PR and SPB-PR

A quantitative comparison of PB-PR, SP-PR and SPB-PR using the RMSE and SSIM metrics defined in Section S4 (Supplement 1), and RT, are presented in Table 1. SPB-PR produces the lowest RMSE and highest SSIM values followed by SP-PR then PB-PR. This is consistent with how closely they match visually to the ground truth in Fig. 4. The same trend is also observed for the SiO₂ shell during shock compression with SPB-PR producing the highest quality reconstruction in terms of RMSE and SSIM followed by SP-PR and PB-PR. Their RMSE and SSIM maps were also computed and are shown in Section S7 (Supplement 1). These calculations exclude the ablation front (see Fig. S3 (Supplement 1)). The reason is, as mentioned in Section 4.3, we suspect that the secondary Fresnel fringes created by the ablation front were recorded outside the x-ray beam profile. For this work, we were not testing these PR methods for their ability to reconstruct phases with parts of the Fresnel fringes outside the FOV. RTs for SP-PR are approximated to the nearest minute while that of PB-PR and SPB-PR were approximated to the nearest half hour increment. RT for PB-PR and SPB-PR varied over several 10's of minutes, even when the total number of iterations and image size were fixed, for different objects and even for different recordings of the same object. The reason is the variable time taken to perform the line search for each iteration. The additional time to reconstruct the phase object with SPB-PR in comparison to PB-PR depends on how often the condition for minimizing f_2 and f_3 is met. This is shown in Section S8 (Supplement 1) where f_2 and f_3 are minimized more frequently when reconstructing the shocked SiO₂ shell than the unshocked SiO₂ shell.

Table 1. RMSE, SSIM and RT measures of reconstructed SiO₂ shell phase maps before and during laser-shock compression. SSIM is in the range [-1 1], where SSIM=1 and SSIM=-1 represent perfect and poor matching to the ground truth [66].

Object	PR method	RMSE (rad)	SSIM	RT (hour)
SiO ₂ shell	SP (Fig. 4(b))	0.79	0.70	0.02
	PB (Fig. 4(c))	1.30	0.68	1.5
	SPB (Fig. 4(d))	0.30	0.91	1.5
Shocked SiO ₂ shell	SP (Fig. 6(b))	7.20	0.90	0.02
	PB (Fig. 6(c))	15.72	0.74	1.5
	SPB (Fig. 6(d))	3.48	0.94	2

5. Conclusions and outlooks

Herein, we developed SPB-PR for recovering the phase of non-absorbing objects from single XPCI images containing both speckle- and propagation-induced x-ray phase contrast. This algorithm leverages both the sensitivity of the former and latter to slowly and rapidly varying features, respectively, to recover object-induced phase shifts spanning over a range of size features. We successfully demonstrated this capability on an xRAGE-simulated XPCI image of a SiO₂ shell before and during laser shock-induced compression. It outperformed two PR methods that use either only the speckle- or propagation-induced x-ray phase contrast by achieving lower RMSE and higher SSIM values. We reproduced the capability of SPB-PR on XPCI images recorded at MEC-LCLS of the same experiment simulated by xRAGE. But, like other differential-based methods, it is susceptible to reconstruction artifacts from unwanted distortions in the reference pattern between recordings with and without the object. It is also worth noting that while SPB-PR was derived under the assumption of a pure phase object, it worked well on weakly attenuating objects. This shows potential for the future use of SPB-PR to better understand and constrain material models for void collapse [21,67], IFE/ICF ablator defect simulations [68,69], as well as other shock-related phenomena such as high explosive detonation [70,71].

Our PR method is underpinned by the objective functions in Eqs. (16a)–(16c), where a combination of numerical methods were implemented for minimizing the objective functions (Section 2.3). The focus of this work was to show that solving Eqs. (16a)–(16c) simultaneously improves PR compared to solving only Eq. (16a) (i.e., PB-PR methods) or Eqs. (16b) and (16c) (i.e., SP-PR methods). However, it would be valuable to investigate other combinations of numerical methods that may achieve greater accuracy and computational speed. This may include, for example, roughness penalties for R_1 (higher order TV [72], BM3D [73], DnCNN [74]), numerical frameworks for solving f_1 (ADMM [75,76], Curvature filter [77]), Poisson noise models [78,79], and image registration methods [80,81]. Equations (16a)–(16c) could also be implemented in a multi-objective optimization algorithm that finds a set of Pareto-optimal solutions. Each solution is optimized for a specific metric, for instance, quantitative accuracy and structural information [82]. Moreover, Pareto optimality provides a more definitive stopping criteria than setting an arbitrary value for the maximum number of iterations, as was employed in our work. This may reduce RT and help mitigate the formation of dark patches as described in Section 4.3.

Finally, the technique introduced here of partitioning the object into slowly and rapidly varying components for retrieving the phase object, can be applied to other differential-based XPCI imaging modalities with significant propagation-induced phase contrast and dark field contrast [2,83,84]. Foams, for example, are widely regarded as a leading solution to scaling up fusion target manufacturing and used in a fusion power plant [85,86]. However, the microstructures of foam is very inhomogeneous, inducing a combination of x-ray attenuation, refraction and small angle scattering. These introduce considerable uncertainties and challenges to modeling implosions because they can seed instabilities and turbulence, which degrades compression and target yield. This work can potentially be incorporated into dark field imaging methods to resolve sub-pixel size features and develop microstructure parameterizations in models and validating against experiments.

Funding. Laboratory Directed Research and Development (20200744PRD1); Fusion Energy Sciences (Early Career Award, 2019); Los Alamos National Laboratory (iHMX, Conventional High Explosives Grand Challenge); National Nuclear Security Administration (DE-NA0003914, DE-NA0004134, DE-NA0003856); U.S. Department of Energy (DE-SC0020229, DE-SC0019329); National Science Foundation (PHY-2020249, PHY-2206380).

Acknowledgments. Use of the Linac Coherent Light Source (LCLS), SLAC National Accelerator Laboratory, is supported by the U.S. Department of Energy, Office of Science, Office of Basic Energy Sciences under Contract No. DE-AC02-76SF00515. AEG, SP, RS, DH acknowledge funding support from DOE ECA-Gleason 2019. Part of this work was performed at the Stanford Nano Shared Facilities (SNSF), supported by the National Science Foundation under award ECCS-2026822.

Disclosures. The authors declare no conflicts of interest.

Data availability. Data underlying the results presented in this paper are not publicly available at this time but may be obtained from the authors upon reasonable request.

Supplemental document. See [Supplement 1](#) for supporting content.

References

1. S. W. Wilkins, T. E. Gureyev, D. Gao, *et al.*, “Phase-contrast imaging using polychromatic hard X-rays,” *Nature* **384**(6607), 335–338 (1996).
2. K. S. Morgan, D. M. Paganin, and K. K. Siu, “X-ray phase imaging with a paper analyzer,” *Appl. Phys. Lett.* **100**(12), 124102 (2012).
3. I. Zanette, T. Zhou, A. Burvall, *et al.*, “Speckle-based x-ray phase-contrast and dark-field imaging with a laboratory source,” *Phys. Rev. Lett.* **112**(25), 253903 (2014).
4. A. F. T. Leong, A. K. Robinson, K. Fezzaa, *et al.*, “Quantitative In Situ Studies of Dynamic Fracture in Brittle Solids Using Dynamic X-ray Phase Contrast Imaging,” *Exp. Mech.* **58**(9), 1423–1437 (2018).
5. D. M. Paganin, H. Labriet, E. Brun, *et al.*, “Single-image geometric-flow x-ray speckle tracking,” *Phys. Rev. A* **98**(5), 053813 (2018).
6. A. F. T. Leong, E. Asare, R. Rex, *et al.*, “Determination of size distributions of non-spherical pores or particles from single x-ray phase contrast images,” *Opt. Express* **27**(12), 17322 (2019).
7. L. Hu, H. Wang, O. Fox, *et al.*, “Fast wavefront sensing for X-ray optics with an alternating speckle tracking technique,” *Opt. Express* **30**(18), 33259 (2022).
8. J. Hagemann, M. Vassholz, H. Hoeppe, *et al.*, “Single-pulse phase-contrast imaging at free-electron lasers in the hard X-ray regime,” *J. Synchrotron Radiat.* **28**(1), 52–63 (2021).
9. A. Burvall, U. Lundström, P. A. C. Takman, *et al.*, “Phase retrieval in X-ray phase-contrast imaging suitable for tomography,” *Opt. Express* **19**(11), 10359–10376 (2011).
10. P. C. Diemoz, F. A. Vittoria, C. K. Hagen, *et al.*, “Single-image phase retrieval using an edge illumination X-ray phase-contrast imaging setup,” *J. Synchrotron Radiat.* **22**(4), 1072–1077 (2015).
11. Y. Liu, M. Seaberg, D. Zhu, *et al.*, “High-accuracy wavefront sensing for x-ray free electron lasers,” *Optica* **5**(8), 967–975 (2018).
12. Z. Wang, K. Ren, X. Shi, *et al.*, “Technical Note: Single-shot phase retrieval method for synchrotron-based high-energy x-ray grating interferometry,” *Med. Phys.* **46**(3), 1317–1322 (2019).
13. K. M. Pavlov, T. E. Gureyev, D. Paganin, *et al.*, “Linear systems with slowly varying transfer functions and their application to x-ray phase-contrast imaging,” *J. Phys. D: Appl. Phys.* **37**(19), 2746–2750 (2004).
14. N. D. Parab, L. Xiong, Q. Guo, *et al.*, “Investigation of dynamic fracture behavior of additively manufactured Al-10Si-Mg using high-speed synchrotron X-ray imaging,” *Addit. Manuf.* **30**, 100878 (2019).
15. M. Kang, W. Li, A. F. Leong, *et al.*, “Crack nucleation and growth during dynamic indentation of chemically-strengthened glass,” *Extreme Mechanics Letters* **38**, 100754 (2020).
16. L. Antonelli, F. Barbato, D. Mancelli, *et al.*, “X-ray phase-contrast imaging for laser-induced shock waves,” *EPL* **125**(3), 35002 (2019).
17. A. F. T. Leong, C. M. Romick, C. A. Bolme, *et al.*, “Quantitative x ray phase contrast imaging of oblique shock wave–interface interactions,” *J. Appl. Phys.* **134**(20), 205901 (2023).
18. T. Carter, S. Baalrud, R. Betti, *et al.*, “Powering the Future: Fusion and Plasmas,” Tech. rep., USDOE Office of Science (SC) (United States) (2020).
19. D. S. Montgomery, “Invited article: X-ray phase contrast imaging in inertial confinement fusion and high energy density research,” *Rev. Sci. Instrum.* **94**(2), 1 (2023).
20. D. S. Clark, M. M. Marinak, C. R. Weber, *et al.*, “Radiation hydrodynamics modeling of the highest compression inertial confinement fusion ignition experiment from the National Ignition Campaign,” *Phys. Plasmas* **22**(2), 22703 (2015).
21. E. M. Escauriza, J. P. Duarte, D. J. Chapman, *et al.*, “Collapse dynamics of spherical cavities in a solid under shock loading,” *Sci. Rep.* **10**(1), 8455 (2020).
22. D. S. Hodge, A. F. T. Leong, S. Pandolfi, *et al.*, “Multi-frame, ultrafast, x-ray microscope for imaging shockwave dynamics,” *Opt. Express* **30**(21), 38405 (2022).
23. M. Vassholz, H. P. Hoeppe, J. Hagemann, *et al.*, “Pump-probe X-ray holographic imaging of laser-induced cavitation bubbles with femtosecond FEL pulses,” *Nat. Commun.* **12**(1), 3468 (2021).
24. F. Wittwer, J. Hagemann, D. Brückner, *et al.*, “Phase retrieval framework for direct reconstruction of the projected refractive index applied to Ptychography and Holography,” *Optica* **9**(3), 295 (2022).
25. T. Latychevskaia, “Iterative phase retrieval for digital holography: tutorial,” *J. Opt. Soc. Am. A* **36**(12), D31 (2019).
26. D. Paganin, *Coherent X-Ray Optics* (Oxford University Press, 2006).
27. M. Born and E. Wolf, *Principles of Optics: Electromagnetic Theory of Propagation, Interference and Diffraction of Light* (Cambridge University Press, 1999), 7th ed.
28. Y. C. Eldar and S. Mendelson, “Phase retrieval: Stability and recovery guarantees,” *Applied and Computational Harmonic Analysis* **36**(3), 473–494 (2014).

29. T. Gureyev, A. Pogany, D. Paganin, *et al.*, “Linear algorithms for phase retrieval in the Fresnel region,” *Opt. Commun.* **231**(1-6), 53–70 (2004).
30. M. A. Beltran, D. M. Paganin, and D. Pelliccia, “Phase-and-amplitude recovery from a single phase-contrast image using partially spatially coherent x-ray radiation,” *J. Opt.* **20**(5), 055605 (2018).
31. D. M. Paganin and K. S. Morgan, “X-ray Fokker–Planck equation for paraxial imaging,” *Sci. Rep.* **9**(1), 17537 (2019).
32. X. Wu and A. Yan, “Phase retrieval from one single phase contrast x-ray image,” *Opt. Express* **17**(13), 11187 (2009).
33. J. P. Guigay, M. Langer, R. Boistel, *et al.*, “Mixed transfer function and transport of intensity approach for phase retrieval in the Fresnel region,” *Opt. Lett.* **32**(12), 1617 (2007).
34. P.-C. Lee, “Phase retrieval method for in-line phase contrast x-ray imaging and denoising by regularization,” *Opt. Express* **23**(8), 10668–10679 (2015).
35. T. Latychevskaia and H.-W. Fink, “Reconstruction of purely absorbing, absorbing and phase-shifting, and strong phase-shifting objects from their single-shot in-line holograms,” *Appl. Opt.* **54**(13), 3925–3932 (2015).
36. D. Paganin, S. C. Mayo, T. E. Gureyev, *et al.*, “Simultaneous phase and amplitude extraction from a single defocused image of a homogeneous object,” *J. Microsc.* **206**(1), 33–40 (2002).
37. M. A. Beltran, D. M. Paganin, K. Uesugi, *et al.*, “2D and 3D X-ray phase retrieval of multi-material objects using a single defocus distance,” *Opt. Express* **18**(7), 6423–6436 (2010).
38. T. E. Gureyev, Y. I. Nesterets, A. W. Stevenson, *et al.*, “Some simple rules for contrast, signal-to-noise and resolution in in-line x-ray phase-contrast imaging,” *Opt. Express* **16**(5), 3223–3241 (2008).
39. S. C. Mayo, P. R. Miller, S. W. Wilkins, *et al.*, “Quantitative x-ray projection microscopy: phase-contrast and multi-spectral imaging,” *J. Microsc.* **207**(2), 79–96 (2002).
40. K. M. Pavlov, H. T. Li, D. M. Paganin, *et al.*, “Single-Shot X-Ray Speckle-Based Imaging of a Single-Material Object,” *Phys. Rev. Appl.* **13**(5), 054023 (2020).
41. T. Latychevskaia and H. W. Fink, “Solution to the twin image problem in holography,” *Phys. Rev. Lett.* **98**(23), 233901 (2007).
42. K. S. Morgan, D. M. Paganin, and K. K. W. Siu, “Quantitative single-exposure x-ray phase contrast imaging using a single attenuation grid,” *Opt. Express* **19**(20), 19781 (2011).
43. I. A. Aloisio, D. M. Paganin, C. A. Wright, *et al.*, “Exploring experimental parameter choice for rapid speckle-tracking phase-contrast X-ray imaging with a paper analyzer,” *J. Synchrotron Radiat.* **22**(5), 1279–1288 (2015).
44. C. Wang, X. Dun, Q. Fu, *et al.*, “Ultra-high resolution coded wavefront sensor,” *Opt. Express* **25**(12), 13736–13746 (2017).
45. M.-C. Zdora, “State of the Art of X-ray Speckle-Based Phase-Contrast and Dark-Field Imaging,” *J. Imaging* **4**(5), 60 (2018).
46. F. Wang, Y. Wang, G. Wei, *et al.*, “Speckle-tracking X-ray phase-contrast imaging for samples with obvious edge-enhancement effect,” *Appl. Phys. Lett.* **111**(17), 174101 (2017).
47. J. Yuan and M. Das, “Transport-of-intensity model for single-mask x-ray differential phase contrast imaging,” *Optica* **11**(4), 478–484 (2024).
48. “Run 19 Machine Parameters Table (PDF),” (2024).
49. S. Ruder, “An overview of gradient descent optimization algorithms,” *arXiv* (2016).
50. T. Vercauteren, X. Pennec, A. Perchant, *et al.*, “Diffeomorphic demons: efficient non-parametric image registration,” *NeuroImage* **45**(1), S61–S72 (2009).
51. I. Roch, P. Bidaud, D. Collard, *et al.*, “Fabrication and characterization of an SU-8 gripper actuated by a shape memory alloy thin film,” *J. Micromech. Microeng.* **13**(2), 330–336 (2003).
52. S. Pandolfi, T. Carver, D. Hodge, *et al.*, “Novel fabrication tools for dynamic compression targets with engineered voids using photolithography methods,” *Rev. Sci. Instrum.* **93**(10), 103502 (2022).
53. X. Wang, P. Rigg, J. Sethian, *et al.*, “The laser shock station in the dynamic compression sector. I,” *Rev. Sci. Instrum.* **90**(5), 053901 (2019).
54. D. McGonegle, P. G. Heighway, M. Sliwa, *et al.*, “Investigating off-Hugoniot states using multi-layer ring-up targets,” *Sci. Rep.* **10**(1), 13172 (2020).
55. D. S. Hodge, S. Pandolfi, Y. Liu, *et al.*, “Visualization of shocked material instabilities using a fast-framing camera and XFEL four-pulse train,” *Proc. SPIE* **11839**, 1183908 (2021).
56. K. Kurzer-Ogul, D. Montgomery, B. Haines, *et al.*, “Radiation and heat transport in divergent shock-bubble interactions,” *Phys. Plasmas* **31**(3), 32304 (2024).
57. M. Gittings, R. Weaver, M. Clover, *et al.*, “The RAGE radiation-hydrodynamic code,” *Comput Sci Disc.* **1**(1), 015005 (2008).
58. I. R. McDonald, “An introduction to equations of state: Theory and applications,” *Phys. Bull.* **38**(10), 391 (1987).
59. R. M. More, K. H. Warren, D. A. Young, *et al.*, “A new quotidian equation of state (QEOS) for hot dense matter,” *Phys. Fluids* **31**(10), 3059–3078 (1988).
60. D. A. Young and E. M. Corey, “A new global equation of state model for hot, dense matter,” *J. Appl. Phys.* **78**(6), 3748–3755 (1995).
61. B. L. Henke, E. M. Gullikson, and J. C. Davis, “X-ray interactions: Photoabsorption, scattering, transmission, and reflection at E = 50–30, 000 eV, Z = 1–92,” *At. Data Nucl. Data Tables* **54**(2), 181–342 (1993).
62. Y. Ding, Z. Huang, and S. A. Ocko, “Transverse-coherence properties of the FEL at the LCLS,” in *32nd International Free Electron Laser Conference* (Stanford Linear Accelerator Center, 2010), pp. 151–154.

63. V. N. Mahajan and G. -M. Dai, "Orthonormal polynomials in wavefront analysis: analytical solution," *J. Opt. Soc. Am. A* **24**(9), 2994 (2007).
64. MATLAB, *version 9.14.0.2254940 (R2023a Update 2)* (The MathWorks Inc., 2014).
65. K. Masaoka, T. Yamashita, Y. Nishida, *et al.*, "Modified slanted-edge method and multidirectional modulation transfer function estimation," *Opt. Express* **22**(5), 6040–6046 (2014).
66. Z. Wang, A. C. Bovik, H. R. Sheikh, *et al.*, "Image quality assessment: From error visibility to structural similarity," *IEEE Trans. on Image Process.* **13**(4), 600–612 (2004).
67. J. S. Lee, B. M. Weon, and J. H. Je, "X-ray phase-contrast imaging of dynamics of complex fluids," *J. Phys. D: Appl. Phys.* **46**(49), 494006 (2013).
68. C. Zulick, Y. Aglitskiy, M. Karasik, *et al.*, "Multimode hydrodynamic instability growth of preimposed isolated defects in ablatively driven foils," *Phys. Rev. Lett.* **125**(5), 055001 (2020).
69. S. C. Miller and V. N. Goncharov, "Instability seeding mechanisms due to internal defects in inertial confinement fusion targets," *Phys. Plasmas* **29**(8), 082701 (2022).
70. N. E. Kerschen, J. D. Drake, C. J. Sorensen, *et al.*, "X-ray phase contrast imaging of the impact of multiple HMX particles in a polymeric matrix," *Propellants, Explos., Pyrotech.* **45**(4), 607–614 (2020).
71. K. B. Wagner, A. Keyhani, A. K. Boddorff, *et al.*, "High-speed x-ray phase contrast imaging and digital image correlation analysis of microscale shock response of an additively manufactured energetic material simulant," *J. Appl. Phys.* **127**(23), 235902 (2020).
72. K. Bredies and M. Holler, "Higher-order total variation approaches and generalisations," *Inverse Problems* **36**(12), 123001 (2020).
73. K. Dabov, A. Foi, V. Katkovnik, *et al.*, "Image denoising by sparse 3-D transform-domain collaborative filtering," *IEEE Trans. on Image Process.* **16**(8), 2080–2095 (2007).
74. K. Zhang, W. Zuo, Y. Chen, *et al.*, "Beyond a Gaussian denoiser: Residual learning of deep CNN for image denoising," *IEEE Trans. on Image Process.* **26**(7), 3142–3155 (2017).
75. U. S. Kamilov, H. Mansour, and B. Wohlberg, "A plug-and-play priors approach for solving nonlinear imaging inverse problems," *IEEE Signal Process. Lett.* **24**(12), 1872–1876 (2017).
76. Z. Allen-Zhu and Y. Li, "NeoN2: Finding local minima via first-order oracles," in *Advances in Neural Information Processing Systems* (2018), pp. 3716–3726.
77. Y. Gong and I. F. Sbalzarini, "Curvature Filters Efficiently Reduce Certain Variational Energies," *IEEE Trans. on Image Process.* **26**(4), 1786–1798 (2017).
78. Z. Li, K. Lange, and J. A. Fessler, "Poisson Phase Retrieval in Very Low-Count Regimes," *IEEE Trans. Comput. Imaging* **8**, 838–850 (2022).
79. V. Katkovnik, "Phase retrieval from noisy data based on sparse approximation of object phase and amplitude," *arXiv* (2017).
80. D. G. Lowe, "Distinctive image features from scale-invariant keypoints," *International Journal of Computer Vision* **60**(2), 91–110 (2004).
81. B. D. de Vos, F. F. Berendsen, M. A. Viergever, *et al.*, "A deep learning framework for unsupervised affine and deformable image registration," *Med. Image Anal.* **52**, 128–143 (2019).
82. M. Abouhawwash and A. M. Alessio, "Multi-Objective evolutionary algorithm for PET image reconstruction: Concept," *IEEE Trans. Med. Imaging* **40**(8), 2142–2151 (2021).
83. M. J. Kitchen, K. M. Pavlov, K. K. W. Siu, *et al.*, "Analyser-based phase contrast image reconstruction using geometrical optics," *Phys. Med. Biol.* **52**(14), 4171–4187 (2007).
84. M. Riedel, K. Taphorn, A. Gustschin, *et al.*, "Comparing x-ray phase-contrast imaging using a Talbot array illuminator to propagation-based imaging for non-homogeneous biomedical samples," *Sci. Rep.* **13**(1), 6996 (2023).
85. V. N. Goncharov, I. V. Igumenshchev, D. R. Harding, *et al.*, "Novel hot-spot ignition designs for inertial confinement fusion with liquid-deuterium-tritium spheres," *Phys. Rev. Lett.* **125**(6), 065001 (2020).
86. R. W. Paddock, H. Martin, R. T. Ruskov, *et al.*, "One-dimensional hydrodynamic simulations of low convergence ratio direct-drive inertial confinement fusion implosions," *Philos. Trans. R. Soc., A* **379**(2189), 20200224 (2021).